Czech Technical University in Prague
Faculty of Nuclear Sciences and Physical Engineering
Department of Physics

A Study of Open Charm Production in p+p Collisions at STAR

by

David Tlustý

Dissertation Thesis Statement

Prague 2014

The dissertation thesis was written during full-time doctoral study at the Department of Physics, Faculty of Nuclear Sciences and Physical Engineering of the Czech Technical University in Prague.

Ph.D. Candidate: David Tlustý
Department of Physics
Faculty of Nuclear Sciences and Physical Engineering
Czech Technical University in Prague
Břehová 9, 110 00 Prague 1, Czech Republic
tlusty@gmail.com

Supervisor: Jaroslav Bielčík
Department of Physics
Faculty of Nuclear Sciences and Physical Engineering
Czech Technical University in Prague
Břehová 9, 110 00 Prague 1, Czech Republic
jaroslav.bielcik@fjfi.cvut.cz

Reviewers: Dr. Elena Bruna

Doc. RNDr. Zdeněk Doležal, DSc.

The dissertation thesis statement was distributed on ....

The defence of the dissertation thesis will be held before the Committee for the presentation and defence of the dissertation thesis in the doctoral degree study program on 18. 12. 2014 at 10:00 in the meeting room No. 111.

In accordance with Para. 9 of Art. 35 of the Study and Examination Code for Students of the CTU, those who are interested may look into the dissertation thesis and make notes, copies, or duplicates from it at their own expense. A copy of the dissertation thesis is available in the Science and Research Office of the Faculty of Nuclear Sciences and Physical Engineering, room No. ......

Doc. RNDr. Vojtěch Petráček, CSc.

Chairman of the Committee for the presentation and defence of the dissertation thesis
Department of Physics
Faculty of Nuclear Sciences and Physical Engineering
Czech Technical University in Prague
Břehová 9, 110 00 Prague 1, Czech Republic

Contents

Abstract

In this work, we present the measurement of D^0 and D^* meson production at mid-rapidity in p+p collisions at $\sqrt{s} = 200$ and 500 GeV. These mesons are reconstructed directly via their hadronic decay channels with daughter particles identified by STAR Time Projection Chamber (TPC) and Time Of Flight (TOF) detectors. These measurements are compared to theoretical model calculations and physics implications are discussed.

1 Introduction

This work deals with the study of open charm hadron production in p+p collisions at $\sqrt{s} = 200$ and $\sqrt{s} = 500$ GeV. This is the first reconstruction of D^0 meson in its hadronic decay channel in p+p collisions at $\sqrt{s} = 200$ GeV. Two independent data analysis were performed (one by author of this thesis) with consistent results and results were published in Ref. [1]. Furthermore the first reconstruction of D^0 and $D^{*\pm}$ meson in p+p collisions at $\sqrt{s} = 500$ GeV were done in this thesis. The proton beams were accelerated by Relativistic Heavy Ion Collider (RHIC) [2], RHIC is located in Brookhaven National Laboratory in Long Island, state New York, and collided at the experiment *Solenoidal Tracker at RHIC* (STAR) [3]. The term open charm denotes hadrons that contain just one constituent charm quark such as $D^0(c\bar{u}), D^+(c\bar{d}), \Lambda_c(cud)$ distinguishing them from the $J/\psi(c\bar{c})$ meson belonging to the group of *heavy quarkonia.* Charm quark as well as bottom quark (generally called heavy quark) production at RHIC energies is dominated by initial gluon fusion and can be described by perturbative QCD (pQCD) due to their large mass [4]. The measurement of the charm quark production in $p + p$ collisions provides both pQCD test and baseline for any measurement in heavy ion collisions.

In relativistic heavy ion collisions at RHIC, heavy quarks are expected to be created from initial hard scatterings. Since heavy quarks have large masses, long life time, and negligible annihilation due to their small population, the number of heavy quarks is conserved during whole medium evolution. The interaction between heavy quarks and the medium is sensitive to the early medium dynamics, therefore heavy quarks are suggested as an ideal probe to quantify the properties of the strongly interacting QCD matter. Furthermore, the production of heavy quarkonia ($J/\psi(c\bar{c}), \Upsilon(b\bar{b})$) in heavy ion collisions is affected by the Debye color screening of the heavy quark potential [5].

The state-of-art measurements of inclusive heavy quark production are carried out through two main approaches:

1. single leptons from open heavy hadron semi-leptonic decays

2. hadrons from hadronic decays

Figure 1 depicts a created pair of charm quarks hadronizing into D^0 and $\overline{D^0}$ with the probability of 56.5%. The Figure further shows the D^0 undergoing a hadronic decay into negative kaon and positive pion with branching ratio of 3.87% and $\overline{D^0}$ undergoing a semi-leptonic decay into a lepton (electron or muon), corresponding neutrino and positive kaon. The branching ratios as well as the hadronization probability are taken from Ref. [6]. This work carries the measurement of the charm quark production through the second approach which albeit suffers from a large combinatorial background (signal to background ratio is on the order of 1/1000), however there's no contribution from other charmed and bottomed hadron decays and there's direct access to open charm meson kinematics owing to the possibility of the D^0 invariant mass reconstruction. This allows to calculate the differential invariant cross section of a D meson production $E\frac{\mathrm{d}^3\sigma_D}{\mathrm{d}p^3} = \frac{\mathrm{d}^2\sigma_D}{2\pi p_T \mathrm{d}p_T \mathrm{d}y}$ at given transverse momentum p_T and rapidity y. The differential invariant cross section of a $c\bar{c}$ production $E\frac{\mathrm{d}^3\sigma_{c\bar{c}}}{\mathrm{d}p^3}$ is then obtained from $E\frac{\mathrm{d}^3\sigma_D}{\mathrm{d}p^3}$ through dividing it by the c quark to open charm hadron probability, albeit the p_T and y are the momentum and rapidity of the open charm hadron respectively.

The charm cross-section can be calculated from an amplitude which is found by summing up the terms of the Feynman diagrams. They have been evaluated at the Next-to-Leading Order (NLO) level [7] including diagrams of orders α_S^2 and α_S^3. The renormalization scale has been chosen near or at the m_q. The $E\frac{\mathrm{d}^3\sigma_{c\bar{c}}}{\mathrm{d}p^3}$ calculation has been extended to the Fixed-Order Next-to-Leading-Log level (FONLL) by including terms of orders $\alpha_S^2\left(\alpha_S \log(p_T/m_q)\right)^k$ (Leading Log) and $\alpha_S^3\left(\alpha_S \log(p_T/m_q)\right)^k$ (Next-to-leading Log) owing to the rise of large logarithms of the ratio p_T/m_q to all orders in the perturbative expansion [8]. The $E\frac{\mathrm{d}^3\sigma_D}{\mathrm{d}p^3}$ has been calculated as

$$E\frac{\mathrm{d}^3\sigma_D}{\mathrm{d}p^3} = \frac{\mathrm{d}^3\sigma_{c\bar{c}}}{\mathrm{d}p^3} \otimes \mathcal{D}(c \to D) \tag{1}$$

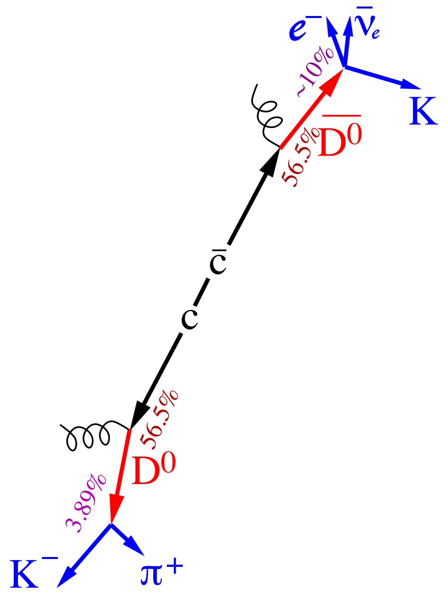

Figure 1: Charm quark fragmentation to D^0 and two main D^0 decay channels.

where the symbol $\otimes$ denotes a generic convolution and $\mathcal{D}(c \to D)$ fragmentation function for the fragmentation of the charm quark into a generic admixture of charm hadrons.

The results of $E\frac{\mathrm{d}^3\sigma_D}{\mathrm{d}p^3}$ and $\frac{\mathrm{d}^3\sigma_{c\bar{c}}}{\mathrm{d}p^3}$ in p+p collisions at $\sqrt{s} = 200$ GeV using the FONLL approach were presented in [4] and the results of $E\frac{\mathrm{d}^3\sigma_D}{\mathrm{d}p^3}$ were confirmed by experimental data presented in [1] based also on analysis discussed in this thesis. The results of $E\frac{\mathrm{d}^3\sigma_D}{\mathrm{d}p^3}$ at $\sqrt{s} = 500$ GeV haven't been published yet and are referred as "private communication" [9]. However they were confirmed by experimental data presented in this thesis.

Let's also note that calculations of the charm cross section at low p_T (< 1 GeV/c) become complicated because charm quarks cannot be treated as a massless flavor. Furthermore, in the low momentum transfer region there is a large uncertainty in the gluon density function, and the strong coupling constant increases dramatically. Thus, pQCD calculations have little predictive power for the total charm cross section in high-energy hadron-hadron collisions [10]. These theoretical issues further demonstrate the necessity of precise experimental measurements to provide constraints that improve theoretical calculations like the one published in [11].

2 Methodology

The $D^0(\overline{D^0})$ undergoes a decay

$$D^0(\overline{D^0}) \xrightarrow{B.R.=3.89\%} K^-\pi^+(K^+\pi^-)$$

with the probability of 3.87% (branching ratio $B.R.$) and mean free path $c\tau \sim 123$ μm. Hence overwhelming majority of D^0 mesons decays inside the RHIC beam pipe, however pions and kaons live long enough to penetrate through all STAR experiment subsystems which have the capability to determine momentum and charge of the pions and kaons (henceforth all other particles) thanks to the STAR magnet [12] and the Time Projection Chamber (TPC) [3]. Additionally, the TPC is able to identify particles through their energy loss per unit length $\mathrm{d}E/\mathrm{d}x$ while penetrating through the TPC gas. The keystone in this analysis was the ability to identify kaons since they are much less abundant than pions. As shown in Figure 2a, TPC can identify kaons for momentum up

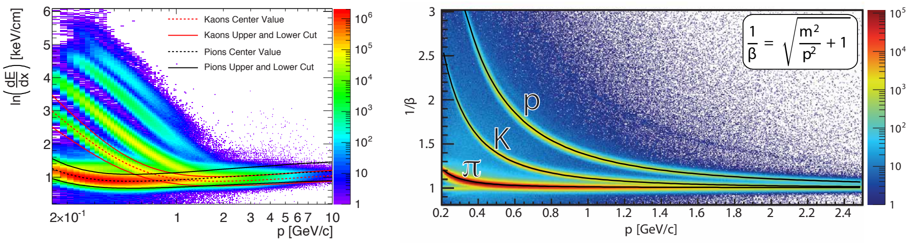

(a) PID trough dE/dx in TPC gas. Lines represent Bichsel parametrization [13] for pions and kaons.

(b) PID trough the time of flight represented by $1/\beta$. Lines represent theoretical prediction shown in the upper right frame.

Figure 2: Particle identification (PID).

to 0.6 GeV/c. With incremental momentum, this ability decreases until completely vanishes around 1.1 GeV/c and further starts to slowly improve owing to the relativistic rise being dependent on the particle mass. The Time Of Flight (TOF) subsystem [14], as demonstrated in Figure 2b, can identify kaons of momenta up to 1.6 GeV/c and separate them from protons up to 3 GeV/c overcoming the critical regions where kaon's dE/dx overlaps pion's and proton's respectively.

The D^0 raw yield was calculated as the area of the gaussian function fitted into the $K^-\pi^+ + K^+\pi^-$ invariant mass spectrum $(M_{K^-\pi^+} + M_{K^+\pi^-})$ after all background had been subtracted in the invariant mass region around expected D^0 mass of 1864.84 MeV/c^2 [6]. D^0 and $\overline{D^0}$ was analyzed together in order to enhance observed signals. Such invariant mass spectrum will be called "Unlike-sign" spectrum in further text. Let's note that the candidates whose rapidity exceeded the (-1,1) interval were rejected. The Unlike-sign spectrum consists of: pairs from $D^0, \overline{D^0}$ decays, pairs from other decays (like $K^{*0}(892)$ for example), and combinatorial background.

The combinatorial background, that constitutes the dominant part of the D^0 candidates invariant mass spectrum, was reconstructed by two independent techniques:

- $\boxed{\text{Like-Sign Method}}$ Pion candidates are paired with the kaon candidates of the same charge. Then the geometric mean of the two subsets (the raw yield of positively $Y_{K^+\pi^+}$ and negatively $Y_{K^-\pi^-}$ charged pairs) is calculated by $2\sqrt{Y_{K^-\pi^-}Y_{K^+\pi^+}}$.

- $\boxed{\text{Rotated Momentum Method}}$ Each pion candidate is paired with the kaon candidate with reversed 3-momentum. Track rotation technique is based on the assumption that by rotating one of the daughter track for 180 degree the decay kinematics is destroyed. Thus the distribution of a pair invariant mass with one track rotated is able to reproduce the random combinatorial background.

The Unlike-sign spectrum is shown in Figure 3 for pairs with p_T between 1.0 and 2.0 GeV/c. The combinatorial background reconstructed by either Like-Sign or Rotated Momentum technique was scaled to match the original Unlike-Sign spectrum of $K\pi$ pairs within the invariant mass interval 1.7 - 1.8 GeV/c^2 and it's shown also in Figure 3, revealing an excellent agreement with the Unlike-sign spectrum. Such agreement allowed to declare that both methods describe combinatorial background well and the background could be subtracted from Unlike-sign spectrum to extract the raw yield of D^0 meson. Results of the background subtractions, let's call them *signal*, are shown also in Figure 3 in the same plot like the Unlike-sign and reconstructed backgrounds, it is zoomed by factor of 2 so that it regards the right scale while the Unlike-sign and combinatorial background regard the left scale. One can see a strong lorentzian peak corresponding to particle $K^{0*}(892)$ (together with its antiparticle), much smaller and wider peak of $K^{2*}(1430)$, and and tiny gaussian peak corresponding to $D^0 + \overline{D^0}$. There's still some residual background, especially between the $K^{0*}(892)$ peak and 0.6 GeV/c^2 corresponding to the beginning of the $K\pi$ phase space, where one can observe a significant peak around 0.7 GeV/c^2 which is $\phi(1019\ \text{MeV}/c^2)$ meson whose one of kaons ($\phi \to K^+K^-$) had been misidentified for pion. Since the invariant mass of the mother particle depends on invariant masses of daughter particles the wrong assignment of mass happening at the particle misidentification causes a shift in the invariant mass of the mother particle. Hence the artificial exchange the kaon for pion causes shift in the invariant mass of the ϕ meson by 355 MeV/c^2.

The $D^{*\pm}$ meson undergoes a cascading decay

$$D^{*\pm} \xrightarrow[p^*=39\ \text{MeV/c}]{B.R.=67.7\%} D^0\pi_S^\pm \xrightarrow{B.R.=3.89\%} K^\mp\pi^\pm\pi_S^\pm$$

with very low decay energy giving both daughter particles momentum in CMS of 39 MeV/c. Hence the difference in invariant mass

$$\Delta M \equiv (M_{K^\mp\pi^\pm\pi^\pm} - M_{K^\mp\pi^\pm}; 1.84 < M_{K^\mp\pi^\pm} < 1.89\ \text{GeV}/c^2)$$

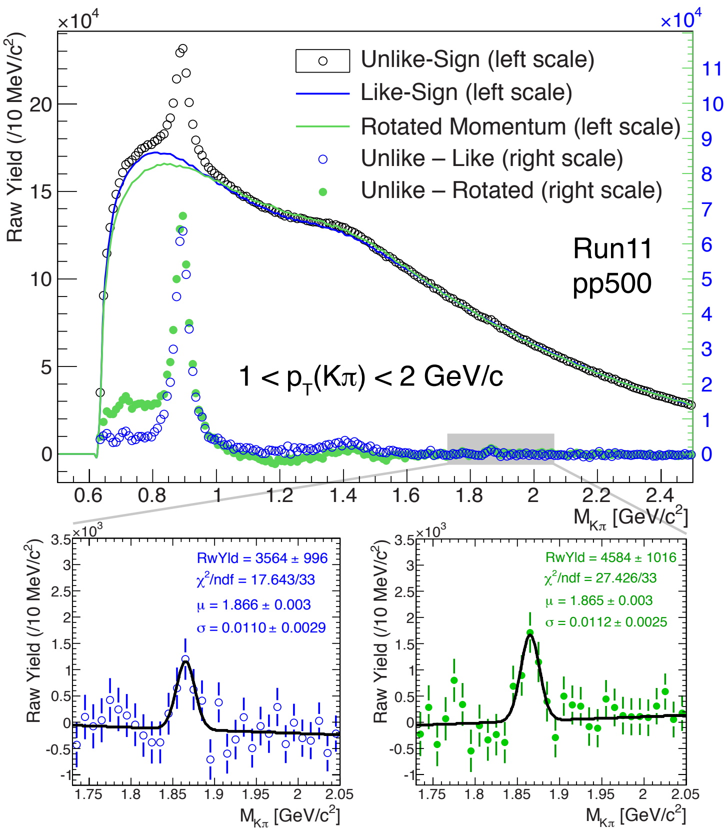

Figure 3: Upper Panel: Opposite-charged $K\pi$ invariant mass with the combinatorial background reconstructed by Like-Sign and Rotated Momentum techniques for all $K\pi$ pairs within $(1.0 < p_T < 2.0$ GeV$/c)$ and $|y(K\pi)| < 1$. The gray rectangle illustrates the zoom to D^0 mass window. Lower left panel: Opposite-charged $K\pi$ pairs invariant mass after Like-Sign background subtracted. Lower right panel: Opposite-charged $K\pi$ pairs invariant mass after Rotated-Momentum background subtracted.

has very low combinatorial background around 145.4 MeV/c^2, which is the difference in mass of the $D^{*\pm}$ and the D^0 meson, and whose resolution is determined by mostly the soft pion π_S momentum resolution. Both factors imply the ability to have a significant peak in ΔM spectrum around 145.4 MeV/c^2. In order to suppress background from jets, the cut $\cos(\theta^*) < 0.77$ was applied on the $K\pi$ pair together with the cut on its invariant mass ($1.84 < M_{K^\mp\pi^\pm} < 1.89$ GeV/c^2) where θ^* is the decay angle of the kaon in the $K\pi$ pair CMS frame. Both cuts are called *kinematical cuts*.

The combinatorial background in ΔM spectrum was reconstructed by two independent techniques:

- $\boxed{\text{Wrong-sign Method}}$ In the triplet of daughter particles, π_S had opposite sign to π.

- $\boxed{\text{Side-band Method}}$ In the triplet of daughter particles, $M_{K^\mp\pi^\pm}$ had been lying between 1.7 and 1.8 or 1.92 and 2.02 GeV/c^2, i. e. outside the D^0 mass window.

The Wrong-sign background yield is contaminated by some real D^* signal whose kaon and pion daughters from D^0 decays are both mis-identified. The fraction of this over counting in the Wrong-sign background is estimated from fast simulation. The Side-band background yield doesn't suffer from this contamination so it was reasonable to use Side-band as the default method for combinatorial background reconstruction and the Wrong-sign (corrected on the over counting) as a cross check.

Figure 4 depicts ΔM denoted as "Right Sign" with both Wrong-sign and Side-band backgrounds and both signal after Wrong-sign and Side-band background subtraction as well as gaussian fits into these signals in $K^\mp\pi^\pm\pi^\pm$ p_T bins.

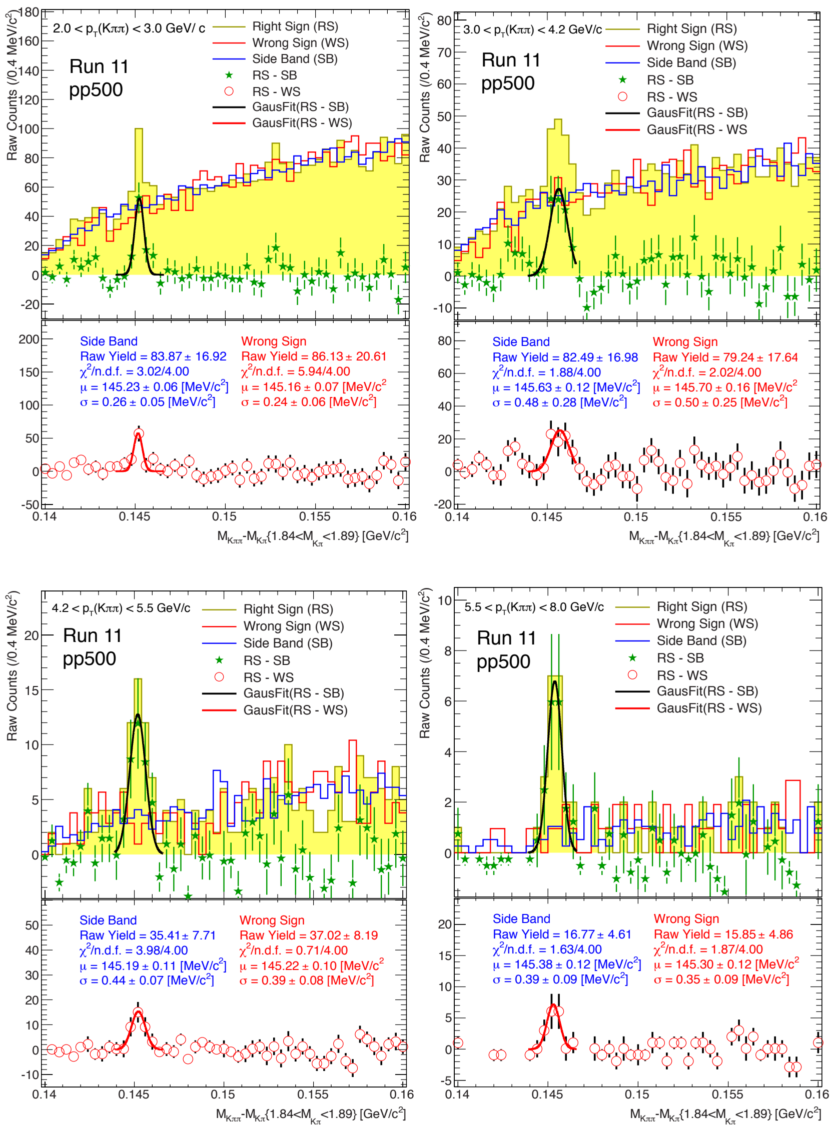

Figure 4: ΔM spectra with combinatorial backgrounds reconstructed by Side-band and Wrong-sign techniques in $K^{\mp}\pi^{\pm}\pi^{\pm}$ p_T bins.

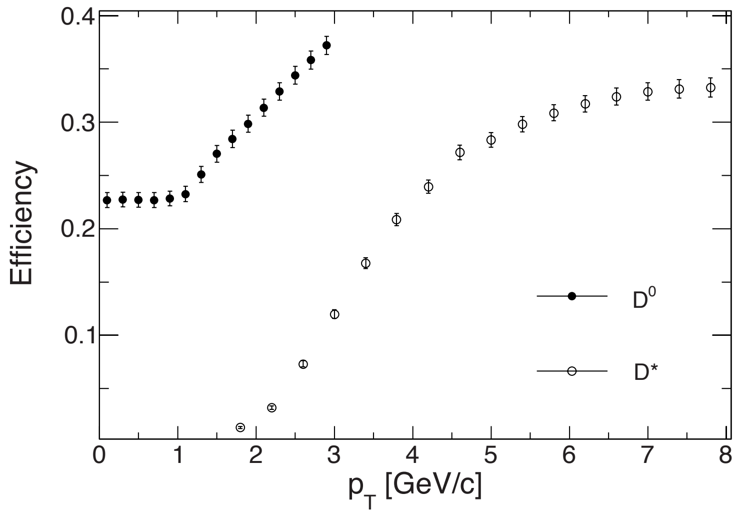

Figure 5: Combined D^0 and D^* reconstruction efficiency versus D^0 and D^* p_T respectively.

Raw yields were corrected on:

- daughter particle track reconstruction efficiency
- daughter particle matching to fast detectors efficiency
- daughter particle identification efficiency
- efficiency of kinematical cuts
- trigger bias

The daughter particle track reconstruction efficiency and the trigger bias were determined trough simulations, the rest from experimental data. Let's note that the correction on the efficiency of kinematical cuts was relevant only in the analysis of D^* mesons. Figure 5 shows combined efficiency of both D^0 and D^* reconstruction as a function of D^0 ($K\pi$) and D^* ($K\pi\pi_S$) p_T respectively. It doesn't include the trigger bias.

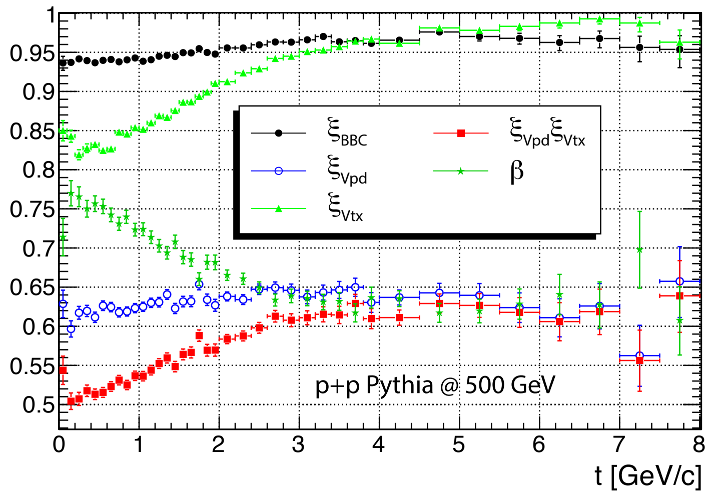

Figure 6: Trigger, Vertex reconstruction efficiency and Trigger Bias.

Heavy quarks are produced during initial hard scatterings creating high p_T particles penetrating easier into calorimeters which makes a higher probability of reconstruction of a collision vertex, thus such events are more likely to enter the analysis. This introduces bias skewed towards events containing charmed particles. Such bias was calculated as a ratio

$$\beta(t) \equiv \frac{\epsilon_{\mathrm{Vpd}}\epsilon_{\mathrm{Vtx}}}{\xi_{\mathrm{Vpd}}(t)\xi_{\mathrm{Vtx}}(t)}, \tag{2}$$

where ϵ_{Vpd} is the VPD trigger efficiency, ϵ_{Vtx} is the efficiency of the collision vertex reconstruction, $\xi_{\mathrm{Vpd}}(t)$ is the VPD trigger efficiency for events containing D^* mesons, $\xi_{\mathrm{Vtx}}(t)$ is the vertex reconstruction efficiency for events containing D^* mesons, and t the transverse momentum of D^* meson. The VPD is Vertex Position Detector [15], coincidental detector consisting of two identical assemblies mounted, covering $4.24 < |\eta| < 5.1$ and providing the minimum bias trigger. Figure 6 shows $\xi_{\mathrm{Vpd}}(t)\xi_{\mathrm{Vtx}}(t)$ together with the Trigger bias $\beta(t)$ calculated according to (2), where $\epsilon_{\mathrm{Vpd}}\epsilon_{\mathrm{Vtx}}$ was found to be 38.82% Let's note that the trigger bias for D^0 was found to be consistent with the trigger bias for D^*.

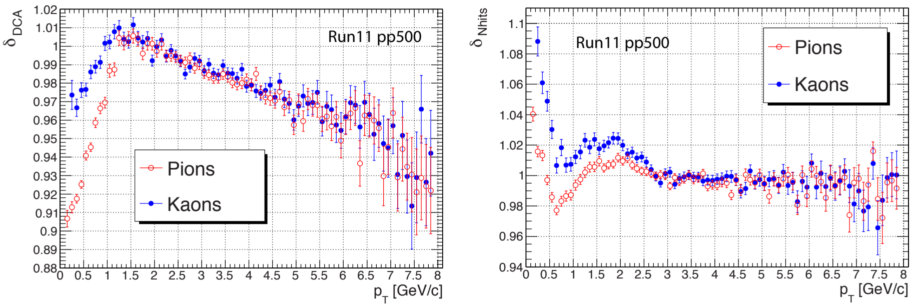

Figure 7: Systematic discrepancy between the data and the embedding.

The absolute (true) reconstruction efficiency in data was unknown, so it was calculated from simulation, which is an approximation. The degree of how the basic track quality distributions (Distance of closest approach to collision vertex - DCA, Number of charge clusters in TPC - Nhits) from simulation matched those from the data represented how good was the approximation. And the difference between them was considered as systematic uncertainty due to this approximation.

It was difficult to calculate the absolute efficiency of the Hhits or DCA from the data, so the relative efficiencies $\varepsilon^{(rel)}_{\text{DCA}}, \varepsilon^{(rel)}_{\text{Nhits}}$ was used instead:

$$\varepsilon^{(rel)}_{\text{DCA}}(p_T) \equiv \frac{\int_0^1 h(p_T, r)\mathrm{d}r}{\int_0^3 h(p_T, r)\mathrm{d}r}, \qquad \varepsilon^{(rel)}_{\text{Nhits}}(p_T) \equiv \frac{\int_{25}^{45} h(p_T, n)\mathrm{d}n}{\int_{15}^{45} h(p_T, n)\mathrm{d}n}, \tag{3}$$

where $h(p_T, r)$ denotes either DCA or Nhits distributions at given p_T. Systematic discrepancy at given p_T was then:

$$\delta_{\text{DCA}}(p_T) \equiv \frac{\varepsilon^{(rel)}_{\text{DCA}}(p_T) \text{ data}}{\varepsilon^{(rel)}_{\text{DCA}}(p_T) \text{ simulation}}, \quad \delta_{\text{Nhits}}(p_T) \equiv \frac{\varepsilon^{(rel)}_{\text{Nhits}}(p_T) \text{ data}}{\varepsilon^{(rel)}_{\text{Nhits}}(p_T) \text{ simulation}} \tag{4}$$

Figure 7 depicts $\delta_{\text{DCA}}(p_T)$ and $\delta_{\text{Nhits}}(p_T)$.

The expected value of the systematic uncertainty from embedding ς in given D^0/D^* transverse momentum bin (a, b) was calculated as the inner product of the discrepancy with the daughter particle p_T distribution $G^{(a,b)}(p_T)$ in the (a, b):

$$\varsigma \equiv \mathrm{E}^{(a,b)}(|1 - \delta(p_T)|) = \int_0^8 |1 - \delta(p_T)| G^{(a,b)}(p_T)\mathrm{d}p_T, \tag{5}$$

(a,b)	$\varsigma_{\mathrm{Nhits}}$ [%]				ς_{DCA} [%]				ς_{tot} [%]
[GeV/c]	K	π	π_S	Sum	K	π	π_S	Sum	
(1.0,2.0)	2.36	0.95		3.32	1.06	3.07		4.13	5.30
(2.0,3.0)	2.14	0.94	3.34	6.42	0.88	2.51	9.16	12.55	14.10
(3.0,4.2)	1.65	0.80	2.00	4.44	0.90	2.08	8.75	11.73	12.54
(4.2,5.5)	1.27	0.70	1.21	3.17	1.13	2.01	8.25	11.39	11.83
(5.5,8.0)	1.01	0.65	1.01	2.67	1.62	2.27	7.22	11.10	11.42

Table 1: Systematic errors from discrepancy between embedded and experimental data. First column presents D^0/D^* transverse momentum bins (a,b) and the last column corresponding systemtic uncertainty obtained from values shown in middle columns by (6).

Results are summarized in Table 1. With the assumption of an ideal correlation among daughter particles's systematic uncertainties, the systematic error on the efficiency determination (and in this analysis also total systematic uncertainty) could have been directly calculated as

$$\varsigma_{\mathrm{tot}} = \sqrt{\left(\sum_{i=1}^{\#\mathrm{daughters}} \varsigma^i_{\mathrm{Nhits}}\right)^2 + \left(\sum_{i=1}^{\#\mathrm{daughters}} \varsigma^i_{\mathrm{DCA}}\right)^2} \tag{6}$$

and is listed in the last column in Table 1.

The contribution from matching efficiency uncertainty was found to be negligible (bellow 3% of ς_{tot}). Let's compare the total uncertainty on the efficiency determination, values in the last column of Table 1, with statistical errors of yields in corresponding D^0/D^* transverse momentum bins (a,b), 17.5% for D^0 (1,2) GeV/c and 21.6%, 20.6%, 21.8%, and 27.5% for D^* (2, 3), (3, 4.2), (4.2, 5.5), and (5.5, 8) GeV/c respectively. In all p_T bins the statistical uncertainty is higher that the total systematic uncertainty from which one can conclude that the whole analysis procedure was good enough for given amount of data. To improve the overall precision of this analysis one can just triple the amount of experimental data to reduce statistical errors to match systematic uncertainties without any change of the analysis procedure.

3 Results

The reconstruction of D^0 in p+p collisions at $\sqrt{s} = 200$ GeV (Run9 pp200 analysis) and reconstruction of D^0 and $D^{*\pm}$ in p+p collisions at $\sqrt{s} = 500$ GeV (Run11 pp500 analysis) at STAR via the hadronic decay channels

$$D^{*\pm} \xrightarrow[p^{*}=39\ \mathrm{MeV/c}]{B.R.=67.7\%} D^0\pi^{\pm} \xrightarrow{B.R.=3.89\%} K^{\mp}\pi^{\pm}\pi^{\pm}$$

$$D^0 \xrightarrow{B.R.=3.89\%} K^{\mp}\pi^{\pm},$$

where $B.R.$ are branching ratios of these open charm mesons to pions and kaons [6], were done. 51.8 million and 107.8 minimum bias events have been analyzed in Run11 pp500 and Run9 pp200 analysis respectively.

This section presents final results of the both p_T-differential and p_T-integrated invariant cross section of charm-anticharm quark pair production at mid-rapidity measurements and total charm-anticharm quark pair cross section estimation using PYTHIA [16] simulation. Let's note that the p_T is transverse momentum of the open charm meson. These results are compared to theoretical model calculations and physics implications are discussed.

The differential invariant cross section $E\dfrac{\mathrm{d}^3\sigma}{\mathrm{d}p^3}$ of an charm quark pair $c\bar{c}$ production at mid-rapidity was calculated according to equation

$$E\frac{\mathrm{d}^3\sigma}{\mathrm{d}p^3}\bigg|_{y=0} = \frac{\mathrm{d}^2\sigma}{2\pi p_T \mathrm{d}p_T \mathrm{d}y}\bigg|_{y=0} = \frac{1}{2}\frac{1}{2\pi}\frac{\sigma^{\mathrm{NSD}}\beta}{N\mathfrak{f}_c\Gamma}\frac{Y}{p_T\Delta p_T\Delta y}\frac{1}{\varepsilon}, \tag{7}$$

where σ^{NSD} is inelastic non-singly diffractive p+p cross section, β is the trigger bias, N is the total number of events entered the analysis, $\mathfrak{f}_c$ represents the ratio of a charm quark hadronizing to an open charm meson, Γ denotes the branching ratio of a decay, and Y is the raw yield in a p_T bin of the width Δp_T within the rapidity window Δy. ε is the combined reconstruction efficiency of the D^0 or D^* reconstruction shown in Figure 5. Results from Run9 pp500 analysis are summarized in Table 2 and results from Run11 pp500 analysis are summarized in Table 3. Both tables show values of all variables used in equation (7). Some variables don't depend on reconstructed D^0/D^* p_T so they are displayed in cells stretched over more columns. Rows between thick horizontal rules show variables and values which are then corrected on bin widths (the bin width correction is discussed further in the text) and plotted in Figures 11, 8, 9, and 10.

σ^{NSD} [mb]	30 ± 3.5	
N	107.8M	
$\mathfrak{f}_c$ [%]	56.5 ± 3.2	
Γ [%]	3.89	
β	0.67	
p_T [GeV/c]	0.8	1.15
Δp_T [GeV/c]	0.4	1.3
Δy	2	
Y	1708±497	1860±635
ε [%]	0.0695	0.0746
$E\frac{\mathrm{d}^3\sigma}{\mathrm{d}p^3}\Big\|_{y=0}$ [nb]	25660 ± 7646	3886 ± 1328
ς_{tot} [%]	6.3	9.8

Table 2: Final results from Run9 pp200 analysis. Table shows values of all variables in equation (7). Some variables don't depend on reconstructed D^0 p_T so they are displayed in cells stretched over more columns. Let's note those results are not corrected on bin widths.

σ^{NSD} [mb]	34 ± 4				
N	51 771 500				
$\mathfrak{f}_c$ [%]	56.5 ± 3.2	22.4 ± 2.8			
Γ [%]	3.89	2.63			
β	0.696	0.652	0.630	0.629	0.636
p_T [GeV/c]	1.5	2.5	3.6	4.85	6.75
Δp_T [GeV/c]	1.0	1.0	1.2	1.3	2.5
Δy	2				
Y	4064 ± 1006	83.9 ± 18.1	82.5 ± 17.0	35.4 ± 7.7	16.8 ± 4.6
$\varepsilon_{\mathrm{tot}}$ [%]	26.2	5.08	17.3	27.5	32.7
$E\frac{\mathrm{d}^3\sigma}{\mathrm{d}p^3}\Big\|_{y=0}$ [nb]	8508 ± 2106	1927 ± 389	312.1 ± 64.25	57.5 ± 12.52	8.674 ± 2.377
ς [%]	5.3	14.1	12.54	11.83	11.42

Table 3: Final results from Run11 pp500 analysis. Table shows values of all variables in equation (7). Some variables don't depend on reconstructed D^0/D^* p_T so they are displayed in cells stretched over more columns. Let's note those results are not corrected on bin widths.

Values of $\mathfrak{f}_c$ and Γ were taken from Ref. [6]. σ^{NSD} was measured for p+p collisions at $\sqrt{s} = 200$ GeV at STAR [17]. There is no such measurement at $\sqrt{s} = 500$ GeV, hence the measured value from p+p collisions at $\sqrt{s} = 200$ GeV was scaled by Pythia with assumption that the systematic error at $\sqrt{s} = 500$ GeV differs negligibly from the one at $\sqrt{s} = 200$ GeV.

Let's note that the p_T values shown in both Tables 3 and 2 were chosen arbitrarily as bin centers because the real values hadn't been known. To know correct p_T values, one must know the exact shape of the $E\frac{\mathrm{d}^3\sigma}{\mathrm{d}p^3}\Big|_{y=0}$ and that had also been unknown. This problem can be solved iteratively. Let's define the new transverse momentum

$$p_T^{(i+1)} = \mathcal{F}^{(i)^{-1}}\left(\int_a^b \mathcal{F}^{(i)}(p_T)\mathrm{d}p_T\right), \tag{8}$$

where $\mathcal{F}^{(i)} \equiv p_T f(p_T)$ with parameters obtained from the $f(p_T)$ fit into $\frac{\mathrm{d}^2\sigma^{(i)}}{2\pi p_T^{(i)}\mathrm{d}p_T\mathrm{d}y}\Big|_{y=0}$ calculated according to (7). $f(p_T)$ is the power law function either of Hagedorn's or Lévy's shape (those power law functions are discussed

Hagedorn's shape		Lévy's shape ($m_0 = 1.5$)		Lévy's shape ($m_0 = 1.27$)	
$p_T^{(6)}$	$E\frac{\mathrm{d}^3\sigma^{(6)}}{\mathrm{d}p^3}\Big\vert_{y=0}$ [mb]	$p_T^{(6)}$	$E\frac{\mathrm{d}^3\sigma^{(6)}}{\mathrm{d}p^3}\Big\vert_{y=0}$ [mb]	$p_T^{(6)}$	$E\frac{\mathrm{d}^3\sigma^{(6)}}{\mathrm{d}p^3}\Big\vert_{y=0}$ [mb]
1.46	$(8.75 \pm 1.53) \cdot 10^{-3}$	1.49	$(8.57 \pm 1.50) \cdot 10^{-3}$	1.49	$(8.60 \pm 1.50) \cdot 10^{-3}$
2.45	$(19.7 \pm 3.97) \cdot 10^{-4}$	2.45	$(19.7 \pm 3.97) \cdot 10^{-4}$	2.45	$(19.7 \pm 3.97) \cdot 10^{-4}$
3.53	$(31.8 \pm 6.55) \cdot 10^{-5}$	3.52	$(31.9 \pm 6.56) \cdot 10^{-5}$	3.53	$(31.9 \pm 6.56) \cdot 10^{-5}$
4.77	$(5.84 \pm 1.27) \cdot 10^{-5}$	4.77	$(5.85 \pm 1.27) \cdot 10^{-5}$	4.77	$(5.85 \pm 1.27) \cdot 10^{-5}$
6.50	$(8.98 \pm 2.47) \cdot 10^{-6}$	6.51	$(8.97 \pm 2.47) \cdot 10^{-6}$	6.51	$(8.97 \pm 2.47) \cdot 10^{-6}$

Table 4: The results after bin width correction having used three differential cross section parametrization: 1) Hagedorn parametrization where $f(p_T) = (10)$; 2) Lévy parametrization where $f(p_T) = (12)$ with $m_0 = 1.5$ GeV/c^2; 3) Lévy parametrization where $f(p_T) = (12)$ with $m_0 = 1.27$ GeV/c^2. $p_T^{(6)}$ is in units GeV/c.

in next paragraphs). $\frac{\mathrm{d}^2\sigma^{(0)}}{2\pi p_T^{(0)}\mathrm{d}p_T\mathrm{d}y}\Big\vert_{y=0}$ and $p_T^{(0)}$ were set to have values from Table 3. After the third iteration the results became very stable. Table 4 exposes results from Run11 pp500 analysis after 6th iteration. The values of the differential invariant cross section after the iterations are model dependent. That's why Table 3 have three main columns dedicated to usage of Hagedorn's and Lévy's shapes. Those main columns have each two sub-columns with the p_T value after the 6th iteration and with the differential invariant cross section after the 6th iteration. Those data are plotted in Figures 8, 9, 10 together with corresponding $f(p_T)$.

Hard scattering amplitudes follow a power-law function giving us assumption of open charm invariant cross section power-law behavior. Long time ago Hagedorn proposed the QCD inspired empirical formula describing the data of the invariant cross section of hadrons as a function of p_T over a wide range [18]:

$$\frac{\mathrm{d}^2\sigma}{p_T\mathrm{d}p_T\mathrm{d}y} = A\left(1 + \frac{p_T}{p_0}\right)^{-n} \longrightarrow \begin{cases} \exp\left(-\frac{np_T}{p_0}\right) & \text{for } p_T \to 0 \\ \left(\frac{p_0}{p_T}\right)^n & \text{for } p_T \to \infty \end{cases} \tag{9}$$

where A, p_0, n are arbitrary constants. This function has indeed become a purely exponential function for small p_T and a purely power law function for large p_T[1]. The mean p_T becomes:

$$\langle p_T \rangle = \frac{A \int_{-\infty}^{\infty} \frac{\mathrm{d}\sigma}{\mathrm{d}y} \mathrm{d}y \int_0^{\infty} p_T^2 \left(1 + \frac{p_T}{p_0}\right)^{-n}}{A \int_{-\infty}^{\infty} \frac{\mathrm{d}\sigma}{\mathrm{d}y} \mathrm{d}y \int_0^{\infty} p_T \left(1 + \frac{p_T}{p_0}\right)^{-n}} = \frac{2p_0}{n-3}$$

The normalization constant A can be obtained from the relation:

$$\mathrm{d}\sigma/\mathrm{d}y = A \int_0^{\infty} p_T \left(1 + \frac{2p_T}{p_0}\right)^{-n} = \frac{Ap_0^2}{(n-1)(n-2)}$$

thus

$$A = 4\frac{\mathrm{d}\sigma}{\mathrm{d}y} \frac{(n-1)(n-2)}{\langle p_T \rangle^2 (n-3)^2}, \qquad p_0 = \frac{\langle p_T \rangle}{2}(n-3)$$

and $c\bar{c}$ invariant cross section can be represented by

$$\frac{\mathrm{d}^2\sigma^{c\bar{c}}}{2\pi p_T \mathrm{d}p_T \mathrm{d}y} = \frac{2}{\pi} \frac{\mathrm{d}\sigma^{c\bar{c}}}{\mathrm{d}y} \frac{(n-1)(n-2)}{\langle p_T \rangle^2 (n-3)^2} \left(1 + \frac{2p_T}{\langle p_T \rangle (n-3)}\right)^{-n} \tag{10}$$

with three free parameters $\mathrm{d}\sigma^{c\bar{c}}/\mathrm{d}y, \langle p_T \rangle, n$ need to be obtained from the least square fit of the real corrected data points.

As an alternative to Hagedorn (9) formula, one can use a different approach based on the Tsallis statistics [19] to fit particle spectra. The Tsallis distribution was derived from a generalized form of the Boltzmann-Gibbs entropy. However, there are other origins discussed in recent days [20] suggesting for example hard collisions approach [21]. The distribution could be written in the form:

$$\frac{\mathrm{d}^2\sigma}{2\pi p_T \mathrm{d}p_T \mathrm{d}y} = C_n \left(1 + \frac{\sqrt{p_T^2 + m_0^2}}{nT}\right)^{-n} \tag{11}$$

[1] It is widely known from experimental data that, as expected from pQCD calculations [22], a pure power law shape successfully describes the high p_T region of particle spectra. At low p_T, suggests a thermal interpretation in which the bulk of the produced particles are emitted by a system in thermal equilibrium with a Boltzmann-Gibbs statistical description of their spectra:

$$E\frac{\mathrm{d}^3\sigma}{\mathrm{d}\mathbf{p}^3} = Ae^{-E/T}$$

where A is a normalization factor and E is the particle energy. At mid-rapidity one can replace E by $m_T = \sqrt{p_T^2 + m_0^2}$, where m_0 is the particle rest mass.

Hagedorn parametrization		
$\left.\frac{\mathrm{d}\sigma}{\mathrm{d}y}\right\|_{y=0} = 272 \pm 77(\mathrm{stat}) \pm 31(\mathrm{sys})\ \mu\mathrm{b}$	$\langle p_T \rangle = 1.14 \pm 0.16$ GeV/c	$n = 13.7 \pm 7.3$
Lévy parametrization with $m_0 = 1.5$ GeV/c^2		
$\left.\frac{\mathrm{d}\sigma}{\mathrm{d}y}\right\|_{y=0} = 211 \pm 43(\mathrm{stat}) \pm 15(\mathrm{sys})\ \mu\mathrm{b}$	$T = 0.19 \pm 0.14$	$n = 8.7 \pm 3.0$
Lévy parametrization with $m_0 = 1.27$ GeV/c^2		
$\left.\frac{\mathrm{d}\sigma}{\mathrm{d}y}\right\|_{y=0} = 216 \pm 45(\mathrm{stat}) \pm 16(\mathrm{sys})\ \mu\mathrm{b}$	$T = 0.25 \pm 0.14$	$n = 9.5 \pm 3.6$

Table 5: The results of fits.

where C_n is the normalization constant, n the power and T an inverse slope parameter.

To calculate C_n, one must integrate (11) over p_T

$$C_n = \frac{1}{\int_0^\infty p_T \left(1 + \frac{\sqrt{p_T^2 + m_0^2}}{nT}\right)^{-n} \mathrm{d}p_T} = \frac{1}{\frac{(nT+m)^{1-n}}{(nT)^{-n}} \frac{m(n-1)+nT}{(n-1)(n-2)}}$$

to get the (11) into the form appropriate to fitting:

$$\frac{\mathrm{d}^2\sigma^{c\bar{c}}}{2\pi p_T \mathrm{d}p_T \mathrm{d}y} = \frac{1}{2\pi} \frac{\mathrm{d}\sigma^{c\bar{c}}}{\mathrm{d}y} \frac{(n-1)(n-2)}{(nT+m_0)[m_0(n-1)+nT]} \left(\frac{nT + \sqrt{p_T^2 + m_0^2}}{nT + m_0}\right)^{-n} \tag{12}$$

with three free fitting parameters $\mathrm{d}\sigma^{c\bar{c}}/\mathrm{d}y, n, T$.

Results of the $f(p_T)$ fits into already p_T bin width corrected data are shown in Table 5. They show strong dependence of the $\left.\frac{\mathrm{d}\sigma}{\mathrm{d}y}\right|_{y=0}$ on the power-law function parametrization. Only 7% of its value and 5% of its statistical error was measured. The rest was got by extrapolation of Hagedorn parametrization of Power-law into zero transverse momentum. Similarly, the extrapolation by Levy parametrization of Power-law accounted for 90% of the $\left.\frac{\mathrm{d}\sigma}{\mathrm{d}y}\right|_{y=0}$ value and 92% of the statistical error. The final result to be published is a combination

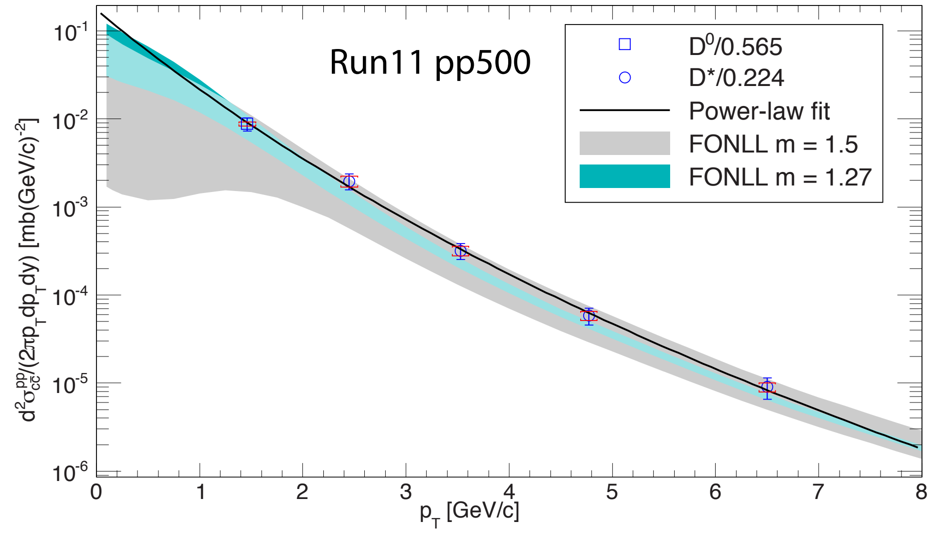

Figure 8: Charm quark production cross section as inferred from D^0 and D^* production in p+p collisions at $\sqrt{s}$ =500 GeV compared with FONLL predictions. The D^0 and D^* data points were divided by the charm quark fragmentation ratios $\mathfrak{f}_c = 0.565$ and $\mathfrak{f}_c = 0.224$ respectively. FONLL calculations [9] used $\mu_R = \mu_F = m_c$ where μ_R is the renormalization scale, μ_F is the factorization scale and m_c is the charm quark mass. "m = 1.5" in the legend denotes $m_c = 1.5$ GeV/c^2 and "m = 1.27" denotes $m_c = 1.27$ GeV/c^2. Data points are already corrected on bin widths and fitted by Hagedorn Power-law function (10).

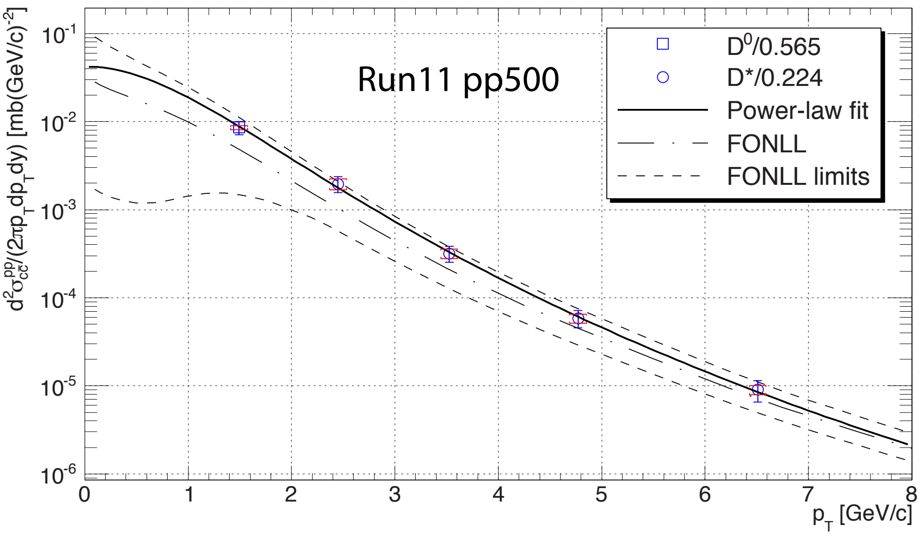

Figure 9: Charm quark production cross section as inferred from D^0 and D^* production in p+p collisions at $\sqrt{s}$ =500 GeV compared with FONLL prediction. The D^0 and D^* data points were divided by the charm quark fragmentation ratios $\mathfrak{f}_c = 0.565$ and $\mathfrak{f}_c = 0.224$ respectively. FONLL prediction [9] used $\mu_R = \mu_F = m_c = 1.5$ GeV/c^2 where μ_R is the renormalization scale, μ_F is the factorization scale and m_c is the charm quark mass. Data points are already corrected on bin widths and fitted by Lévy Power-law function (12) with m_0 chosen to be 1.5 GeV/c^2.

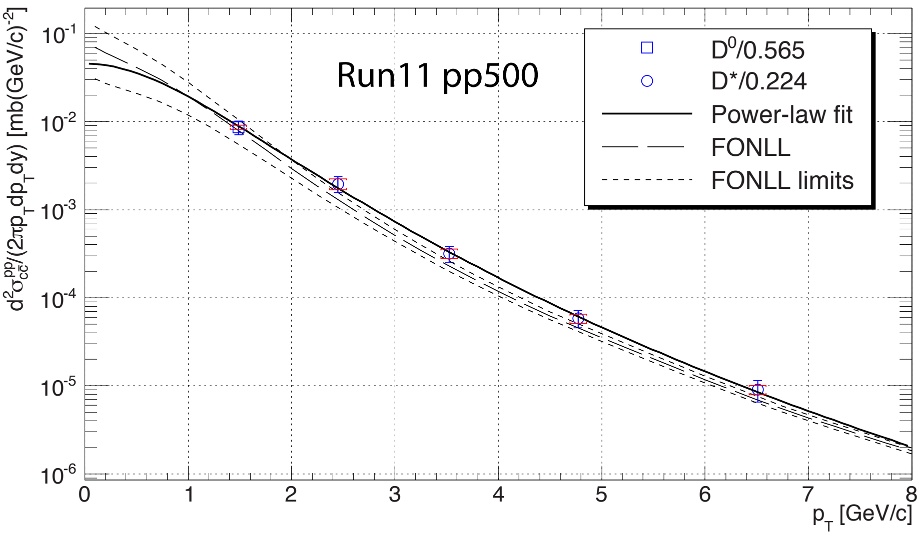

Figure 10: Charm quark production cross section as inferred from D^0 and D^* production in p+p collisions at $\sqrt{s}$ =500 GeV compared with FONLL prediction. The D^0 and D^* data points were divided by the charm quark fragmentation ratios $\mathfrak{f}_c = 0.565$ and $\mathfrak{f}_c = 0.224$ respectively. FONLL prediction [9] used $\mu_R = \mu_F = m_c = 1.27$ GeV/c^2 where μ_R is the renormalization scale, μ_F is the factorization scale and m_c is the charm quark mass. Data points are already corrected on bin widths and fitted by Lévy Power-law function (12) with m_0 chosen to be 1.27 GeV/c^2.

of the result obtained with the help of Hagedorn parametrization (bin with correction and extrapolation to zero p_T) and Lévy parametrization with $m_0 =$ 1.5 GeV/c^2. Lévy parametrization with m_0 = 1.27 GeV/c^2 gives very similar result to the one with m_0 = 1.5 GeV/c^2, so the Lévy does not have to be counted twice. Both Lévy and Hagedorn parametrization were fitted into the same data points, which implicates that 8% of 43 μb (statistical error from Lévy extrapolation) and 5% of 77 μb (statistical error from Hagedorn extrapolation) are correlated with correlation coefficient to be 1. The rest of statistical errors are totally independent with correlation coefficient to be 0. Based on article [24], it was found that the correlated part of the statistical error was too small to have any significant impact. The final result was thus calculated as weighted average of $\left.\frac{\mathrm{d}\sigma}{\mathrm{d}y}\right|_{y=0}$ determined using the Hagedorn parametrization and $\left.\frac{\mathrm{d}\sigma}{\mathrm{d}y}\right|_{y=0}$ determined using the Lévy parametrization with m_0=1.5 GeV/c^2 since both are independent. Lévy parametrization with m_0=1.27 GeV/c^2 is correlated with the m_0=1.5 GeV/c^2 one. Thus the m_0=1.5 GeV/c^2 one was picked arbitrarily, because it matches the measured points better. The extrapolated bin-by-bin systematic errors were treated the same way as values. All of this above gives the final result:

$$\left.\frac{\mathrm{d}\sigma}{\mathrm{d}y}\right|_{y=0} = 225 \pm 38(\mathrm{stat}) \pm 19(\mathrm{sys}) \pm 26(\mathrm{norm})\ \mu\mathrm{b} \tag{13}$$

where the term "norm" denotes error non-singly-diffractive cross section. The errors of $\mathfrak{f}_c$ have not been propagated into the final result yet. The Run11 pp500 analysis results are still presented as preliminary.

The charm cross section at mid rapidity was extrapolated to full rapidity using two different sets of PYTHIA simulation parameters. The extrapolation factor was found to be 5.6 ± 0.1 giving the total charm production cross section value:

$$\sigma_{c\bar{c}}^{pp} = 1260 \pm 211(\mathrm{stat}) \pm 109(\mathrm{sys}) \pm 146(\mathrm{norm})\ \mu\mathrm{b} \tag{14}$$

This result is displayed with results from other experiments in Figure 12, revealing very good agreement with NLO prediction [23].

In the Run9 pp200 analysis, only Hagedorn's shape power law function was used to fit to the data points. The $\left.E\frac{\mathrm{d}^3\sigma}{\mathrm{d}p^3}\right|_{y=0}$ from Run9 pp200 analysis is shown in Figure 11. The black triangles together with black circles represent results published in [1] and green triangles results of author's D^0 production cross check analysis. The published $c\bar{c}$ production cross section at mid-rapidity is

$$\left.\frac{\mathrm{d}\sigma}{\mathrm{d}y}\right|_{y=0} = 170 \pm 45(\mathrm{stat})^{+38}_{-59}(\mathrm{sys})\ \mu\mathrm{b} \tag{15}$$

The charm cross section at mid-rapidity (15) was extrapolated to full phase space using the same extrapolation factor, 4.7 ± 0.7, as in [?], and the extracted charm total cross section at $\sqrt{s} = 200$ GeV is

$$\sigma^{pp}_{c\bar{c}} = 797 \pm 210(\mathrm{stat})^{+208}_{-295}(\mathrm{sys})\ \mu\mathrm{b} \tag{16}$$

The value (16) is also displayed in Figure 12.

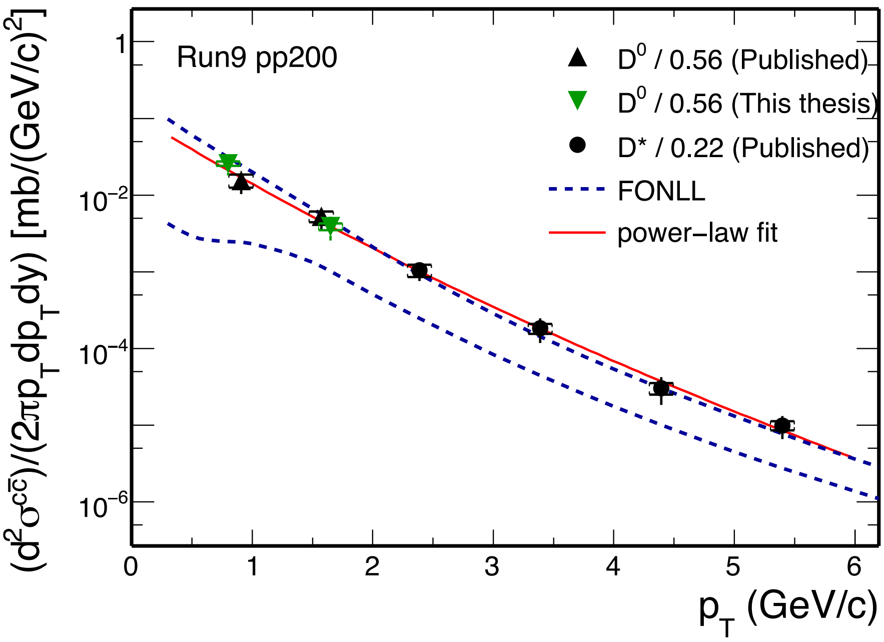

Figure 11: Charm quark production cross section as inferred from D^0 and D^* production in p+p collisions at $\sqrt{s}$ =200 GeV compared with FONLL calculation [8]. The D^0 and D^* data points were divided by the charm quark fragmentation ratios $\mathfrak{f}_c = 0.565$ and $\mathfrak{f}_c = 0.224$ respectively. D^0 data points from this analysis are shown as green triangles, compared with results from [1] having the tag "(Published)" in the legend. Data points are already corrected on bin widths and fitted by Hagedorn Power-law function (10).

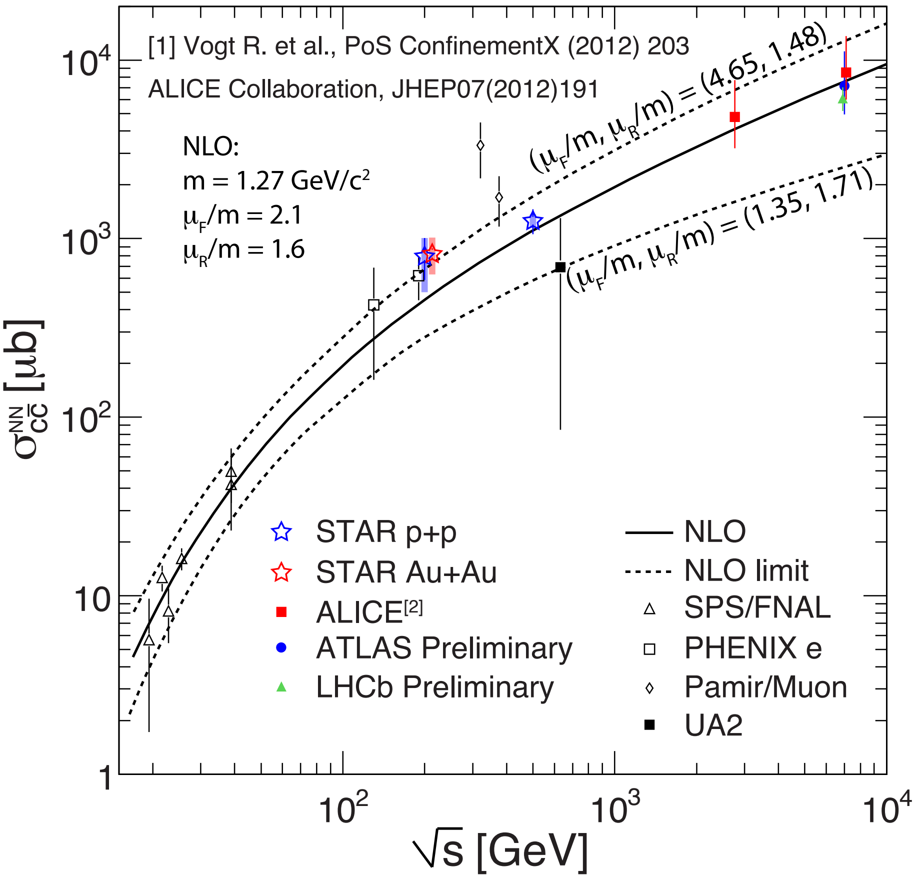

Figure 12: Total Charm quark production cross section as a function of Centre-of-mass collision energy $\sqrt{s}$.

4 Summary

In summary, the first measurement of the charm pair production cross section in p+p collisions at RHIC at $\sqrt{s} = 500$ GeV and 200 GeV has been reported. The cross section was calculated from the production of open charmed-meson D^0 and D^* reconstructed via their hadronic decays, covering the p_T range from 1 to 8 GeV/c. The measured transverse momentum differential cross section is consistent with the prediction of a Fixed-Order Next-to-Leading Logarithm perturbative QCD calculation. The charm pair production cross section at mid-rapidity is measured to be

$$\left.\frac{\mathrm{d}\sigma}{\mathrm{d}y}\right|_{y=0} = 225 \pm 38(\mathrm{stat}) \pm 19(\mathrm{sys}) \pm 26(\mathrm{norm})\ \mu\mathrm{b}$$

in p+p collisions at $\sqrt{s} = 500$ GeV and

$$\left.\frac{\mathrm{d}\sigma}{\mathrm{d}y}\right|_{y=0} = 170 \pm 45(\mathrm{stat})^{+38}_{-59}(\mathrm{sys})\ \mu\mathrm{b}$$

in p+p collisions at $\sqrt{s} = 200$ GeV. The total charm pair cross section is estimated as

$$\sigma^{pp}_{c\bar{c}} = 1260 \pm 211(\mathrm{stat}) \pm 109(\mathrm{sys}) \pm 146(\mathrm{norm})\ \mu\mathrm{b}$$

in p+p collisions at $\sqrt{s} = 500$ GeV and

$$\sigma^{pp}_{c\bar{c}} = 797 \pm 210(\mathrm{stat})^{+208}_{-295}(\mathrm{sys})\ \mu\mathrm{b}$$

in p+p collisions at $\sqrt{s} = 200$ GeV. Results measured at both energies are consistent with Next-To-Leading order perturbative QCD calculation.

The results of D^0/D^* production analysis in p+p collisions at $\sqrt{s} = 200$ GeV have been already used as the baseline for the D^0 suppression in Au+Au collisions at $\sqrt{s_{\mathrm{NN}}} = 200$ GeV measurement published in Ref. [25]. The suppression in the most central Au+Au collisions was compared to various models and it was found that the calculations including a substantial amount of charm-medium interaction and hadronization via both fragmentation and coalescence describe the measured D^0 meson nuclear modification factor R_{AA} well.

STAR has been recently upgraded with two new detectors, the Heavy Flavor Tracker (HFT) [26] and Muon Telescope Detector (MTD) [27]. The HFT is based on cutting edge silicon detector technologies with excellent position resolutions and low material budgets. It provides STAR with the capability of identifying heavy-flavor particles and distinguishing between charm and bottom on an event-by-event basis through track impact parameter measurements [28]. The MTD enables STAR to identify high p_T muons for the first time, which is important for quarkonium measurements in di-muon decay channels and for open heavy-flavor measurements through e. g. electron-muon correlations. With the additions of the HFT and MTD, STAR is in an excellent position for heavy-flavor measurements with unprecedented precisions in the coming years.

References

[1] L. Adamczyk *et al.*, Phys. Rev. D **86**, 072013 (2012).

[2] H. Hahn *et al.*, Nucl. Inst. Meth. A **499**, 245 (2003).

[3] K. H. Ackermann *et al.*, Nucl. Instrum. Meth. A **499**, 624 (2003).

[4] M. Cacciari, P. Nason and R. Vogt, Phys. Rev. Lett. **95**, 122001 (2005).

[5] T. Matsui and H. Satz, Phys Lett. B **178**, 416 (1986).

[6] J. Beringer *et al.*, Phys. Rev. D **86**, 010001 (2012).

[7] P. Nason and S. Dawson, Nucl. Phys. B. **303**, 607 (1988).

[8] M. Cacciari, M. Greco, and P. Nason, Jour. High Energy Phys. **05**, 007 (1998).

[9] R. Vogt, private communication (2012).

[10] R. Vogt, Eur. Phys. J. Special Topics **155**, 213 (2008).

[11] R. Vogt *et al.*, Phys. Rev. C **87**, 014908 (2013).

[12] R. L. Brown, A. Etkin, K. J. Foley *et al.*, The STAR Detector Magnet Subsystem, in Particle Accelerator Conference, 1997. Proceedings of the 1997, vol. **3** 32303232 (1997).

[13] H. Bichsel, Nucl. Instrum. Meth. A **562**, 154 (2006).

[14] Letter of Intent, RICE-TOF Group, Proposal for a single tray of MRPC-TOF for STAR, 2001-6 (2004).

[15] W. J. Llope *et al.*, The STAR Vertex Position Detector, arXiv:1403.6855 (2014).

[16] T. Sjöstrand, http://home.thep.lu.se/∼torbjorn/Pythia.html (2014).

[17] http://www.star.bnl.gov/protected/highpt/dunlop/pp/normalization (2014).

[18] Riv. Nuovo Cim. **6N10**, 1-50 CERN-TH-3684 (1984).

[19] C. Tsallis, J. Stat. Phys. **52** 479 (1988).

[20] G. Wilk and Z. Wlodarczyk, Eur. Phys. J. A **40** 299 (2009).

[21] G. Wilk and Ch. Wong, Phys. Rev. D **87**, 114007 (2013).

[22] D. de Florian and R. Sassot, Phys. Rev. D **69**, 074028 (2004).

[23] Vogt R. *et al.*, PoS ConfinementX 203 (2012).

[24] P. Avery, "Combining Measurements with Correlated Errors", CBX 95-55 (1996).

[25] L. Adamczyk *et al.*, Phys. Rev. Lett. **113** 142301 (2014).

[26] Technical Design Report: The STAR Heavy Flavor Tracker (2011).

[27] L. Ruan *et al.*, J. Phys. G: Nucl. Part. Phys. **36**, 095001 (2009).

[28] Y.Zhang *et al.*, J. Phys. G: Nucl. Part. Phys. **41**, 025103 (2014).